

Elastic Instabilities Govern the Morphogenesis of the Optic Cup

Jeong-Ho Lee¹, Harold S. Park,^{*} and Douglas P. Holmes^{1,†}

Department of Mechanical Engineering, Boston University, Boston, Massachusetts 02215, USA

 (Received 2 March 2021; accepted 6 August 2021; published 23 September 2021)

Because the normal operation of the eye depends on sensitive morphogenetic processes for its eventual shape, developmental flaws can lead to wide-ranging ocular defects. However, the physical processes and mechanisms governing ocular morphogenesis are not well understood. Here, using analytical theory and nonlinear shell finite-element simulations, we show, for optic vesicles experiencing matrix-constrained growth, that elastic instabilities govern the optic cup morphogenesis. By capturing the stress amplification owing to mass increase during growth, we show that the morphogenesis is driven by two elastic instabilities analogous to the snap through in spherical shells, where the second instability is sensitive to the optic cup geometry. In particular, if the optic vesicle is too slender, it will buckle and break axisymmetry, thus, preventing normal development. Our results shed light on the morphogenetic mechanisms governing the formation of a functional biological system and the role of elastic instabilities in the shape selection of soft biological structures.

DOI: 10.1103/PhysRevLett.127.138102

Eye development is a complex, multiscale morphogenetic process that couples cell growth, division, and biological signaling at cellular scales, with large deformation and shape changes. The eye organogenesis begins with formation of the optic vesicles (OVs), nearly spherical shells that undergo invagination—a process that locally reverses the curvature of tissues from convex to concave [1], to form the optic cup (OC), a cavity that eventually houses the eye. It is well established that many congenital eye disorders arise from disruptions in embryonic eye development, including anophthalmia or microphthalmia [2], aniridia [3], coloboma [4], retinal dysplasia [5], and retinal detachment [6].

In the embryonic stage of eye development, the OV bilaterally protrudes from the forebrain and contacts the surface ectoderm (SE). The OV and the SE epithelium are attached to each other through the stiff extracellular matrix (ECM) secreted by both SE and OV, which thickens to form the lens placode and retinal placode. These placodes invaginate, such that curvature of the inner portion of the OV (IOV) changes sign compared to its outer portion (OOV) as shown in Fig. 1(a), to form the lens vesicle and OC, respectively [7,8]. Despite recent efforts [9,10], important questions remain open as to what mechanisms govern OC morphogenesis during and after invagination [5,11–17] and how growth of the IOV and OOV, and evolution of their mechanical properties, impact the morphogenetic processes.

In this Letter, we advance two novel points that contribute to the physics of OC morphogenesis. First, the morphogenetic process is driven by two elastic instabilities that are analogous to snap-through instabilities in spherical shells. These occur at different times during OC

development, corresponding to invagination and rapid deepening observed in biological experiments [13,18]. Second, we demonstrate that the second morphogenetic instability is sensitive to OC geometry. Specifically, for certain geometries, the OC buckles rather than snaps during the second instability, which breaks axisymmetry, and prevents normal OC morphogenesis. This result suggests that some congenital eye disorders, such as glaucoma in newborn infants [19], may be due to OC geometry during morphogenesis.

The OV geometry motivates a simplification of their initial shape to a spherical shell. The ECM and IOV form a

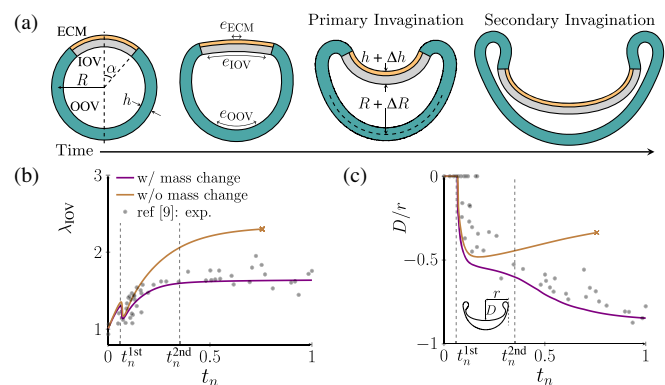


FIG. 1. (a) Simplified schematic of the OC morphogenesis. (b) Thickness change ratio of IOV center wall λ_{IOV} as function of the normalized time t_n . (c) Invagination depth D normalized by OC horizontal radius r as function of t_n . (b) and (c) show comparisons of our model with existing experimental data [9], using $R/h = 5$ and $\alpha = 40^\circ$ with primary and secondary invagination at t_n^{1st} and t_n^{2nd} .

bilayer cap that subtends an opening angle α , while the OOV is a monolayer covering the rest of the sphere [Fig. 1(a)]. We modeled the mechanical response of the OC as a multilayer Kirchhoff-Love (KL) shell [20], which assumes the 3D shell may be represented by its 2D midsurface. Each layer of the KL shell (ECM, IOV, and OOV) is, in contrast to recent works using shells to study biological morphogenesis [29–31], allowed to undergo large strains and rotations and change thickness, via the plane-stress condition, during deformation while being modeled by a compressible neo-Hookean material model [32,33], which takes the energy density form $\Psi_0 = (\lambda/4)(J_m^2 - 1 - 2 \log J_m) + (\mu/2)(I_{m1} - 3 - 2 \log J_m)$ with Lamé constants λ and μ , and invariants I_{m1} and J_m of the elastic right Cauchy-Green tensor. To account for large strains and rotations during growth, we utilize the well-established multiplicative decomposition of deformation gradient \mathbf{F} into growth \mathbf{F}_g and elastic deformation \mathbf{F}_m parts [34–37]. Each layer of the OC is subject to isotropic area growth via $\mathbf{F}_g = (e, e, 1)$ where e is the in-plane expansion factor due to growth [20]. We simulate the OC formation process by solving two coupled balance equations: linear momentum balance to determine elastic deformation via \mathbf{F}_m and mass balance to account for growth via \mathbf{F}_g . These equations are solved numerically using the isogeometric analysis method, a modern finite-element-like method that is well suited for shell problems due to its ability to provide an accurate shell midsurface description [38].

We model the differential growth during OC formation by imposing different mass sources on the ECM, IOV, and OOV in the manner of density-preserving growth [9], such that the three regions have different (experimentally measured) growth rates [9], i.e., $e_{\text{ECM}}(t_n) = 1$, $e_{\text{IOV}}(t_n) = 1 + 5t_n$, and $e_{\text{OOV}}(t_n) = 1 + 1.5t_n$ as a function of the normalized time $t_n = t/\tau$, where $\tau = 20$ hours is the experimentally measured time-scale for OC morphogenesis. The fluidlike components surrounding the OV are neglected [39–41], based on previous studies showing that instabilities of spherical shells are not suppressed by the surrounding fluid environment [42].

A critical, but often neglected, feature in morphogenetic modeling is the effect that mass addition during growth has on the state of stress of the growing body. We find that [see Supplemental Material (SM) for detailed derivation [20]], if the added material during density-preserving growth is the same as the existing material in the body, the stress Σ^{ij} generated in the growing body is amplified as

$$\Sigma^{ij} = e^2 \frac{\partial \Psi_0}{\partial \epsilon_{ij}}, \quad (1)$$

where Ψ_0 is the neo-Hookean strain energy density, and ϵ_{ij} is the strain tensor. Thus, e^2 acts as a stress amplification

factor on the internal stress due to mass change from growth, in which $\partial \Psi_0 / \partial \epsilon_{ij}$ is the standard representation for the internal stress [43]. This stress amplification factor e^2 generalizes previous works [44], as shown in the SM [20].

First, we show that our computational model can capture existing experimental data for OC morphogenesis in a chick embryo [9,10], as shown in Figs. 1(b) and 1(c). The geometric and material parameters for the chick OVs followed previous experiments [9,10,45], i.e., opening angle $\alpha = 40^\circ$, initial radius (R) of $50 \mu\text{m}$, and radius to total thickness ratio (R/h) of 5. The bilayer cap has ECM thickness (h^{ECM}) of $h/10$ and IOV thickness (h^{IOV}) of $9h/10$ whose ratio is $m = h^{\text{ECM}}/h^{\text{IOV}} = 1/9$, and the monolayer OOV has thickness (h^{OOV}) of h . The shear moduli for the ECM and the IOV and OOV are 11 kPa (μ^{ECM}) and 220 Pa (μ^{IOV} and μ^{OOV}), respectively, whose ratio is $n = \mu^{\text{ECM}}/\mu^{\text{IOV}} = 50$ on the bilayer cap. Poisson's ratio for all regions was set to $\nu = 0.45$ based on biologically observed data showing that eye tissue is not incompressible [46,47].

Figures 1(b) and 1(c) show the simulation results of OC formation with and without accounting for the effect of mass change during growth on the stress, where neglecting the mass change corresponds to taking $e^2 \rightarrow 1$ in (1). By comparing to the experimental results [9], it is clear that our model accurately captures the evolution of thickness change ratio of the IOV center wall (λ_{IOV}) as well as invagination depth (D) normalized by OC horizontal radius (r), which are geometric parameters that characterize the OC size and shape. Therefore, the stress amplification from mass addition significantly impacts the local and inhomogeneous growth and enables the accurate simulation of experimentally observed OC growth. This also demonstrates that there is no need to prescribe hypothetical stiffness or growth property gradients as in previous OC growth modeling [9,10].

The OV thickness is known to vary with diverse biological cues, such as protein-2 alpha [48–50], which implies that the radius-thickness ratio R/h of initial OC shape also varies with different biological situations. To account for these unknown thickness variations, we performed numerical simulations at $\alpha = 40^\circ$ with different R/h within the biologically relevant range (5 to 20) [51–53]. This initial geometry is characterized using a single, dimensionless parameter $\bar{\theta} = \alpha \sqrt{R/h}$, which describes the depth and slenderness of the bilayer cap region relative to the angular width of the boundary layer [54].

For all values of $\bar{\theta}$ examined, the shells exhibit two distinct shape-shifting events (Fig. 2). At early times, the apex of the OC inverts, resulting in the formation of a cuplike shape, which we refer to as primary invagination (Fig. 2, $i \rightarrow ii$, $I \rightarrow II$). As t_n increases, we observe a second shape-shifting event that is sensitive to the initial

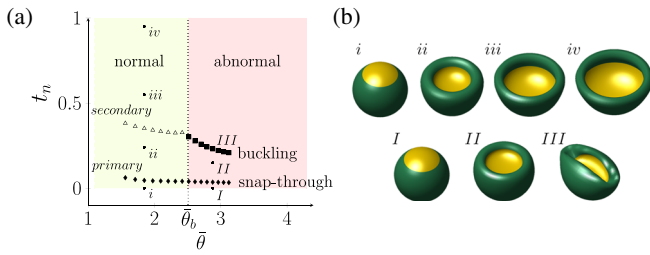


FIG. 2. (a) Simulation results varying R/h at $\alpha = 40^\circ$, considering mass changes. Diamond means the first instability point while triangle and square are the second instability. At $\bar{\theta} = 2.51$ ($\bar{\theta}_b$), the shape-morphing mechanism changes from secondary invagination (triangle) to buckling (square). (b) Representative OC formation process: normal OC (top row) and abnormal OC shape due to buckling (bottom row).

geometry. For lower $\bar{\theta}$, i.e., thicker shells, we observe a rapid deepening of the OC which preserves axisymmetry—we refer to this as secondary invagination (Fig. 2, $ii \rightarrow iii$). For higher $\bar{\theta}$, i.e., thinner shells, we observe that the second shape-shifting event consists of a loss of axisymmetry (Fig. 2, $II \rightarrow III$). We note that, for simulations that neglect mass changes, the symmetry-breaking event ($II \rightarrow III$) occurred for all $\bar{\theta}$, which means the normal morphogenesis process resulting in an axisymmetric OC cannot be modeled without mass addition. See SM [20] for OC formation movies.

To analyze, rationalize, and predict the qualitative features underlying the different shape-morphing pathways of OC morphogenesis, we used a shell model which accounts for growth as a stimulus that changes the rest length, i.e., natural stretch, and curvature, i.e., natural curvature of the shell's midsurface. The strain energy stored in the shell during growth is estimated based on updated rest midsurfaces. As a result, the natural curvature in the cap acts like a torque along the intersection between the cap and OOV to deform the OC [20]. When these natural quantities are homogeneous over some segment of shells, they can be represented by scalar values of Λ (stretch) and κ (curvature) whose specific values are calculated for each segment of the OC based on the experimentally measured growth characteristics (see SM for detailed derivation [20]), i.e., e_{ECM} and e_{IOV} for the bilayer cap, and e_{OOV} for the OOV. As a result, the cap and OOV have their own scalar values of natural stretch and curvature. The presence of Λ and κ imparts residual stresses in the growing OC, and these quantities play a similar role as external loads and torques do in classical mechanics, which can destabilize shells [55,56]. This suggests that OC morphogenesis may be governed by instabilities which result from residual stress that builds up during growth.

In the cap region, experimental observations note that the ECM and IOV grow at different rates. This through-thickness differential growth induces a natural curvature

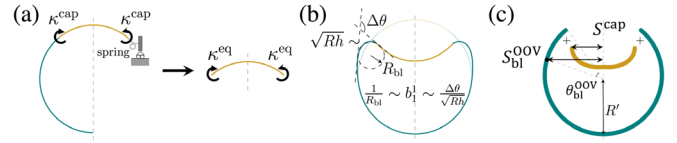


FIG. 3. (a) Equivalent natural curvature. (b) Geometrical characteristics on the OOV bending-dominated boundary layer. (c) Characteristic span of each separated cap and OOV.

that changes the apex of the OC from convex to concave. However, the inversion of this cap is resisted by the OOV which is a monolayer growing homogeneously and has to bend to accommodate the deforming cap. Open spherical shells experiencing an evolving natural curvature may exhibit a snap-through instability that everts the shell at a critical curvature [55]. Here, the OC is not an open shell, as the deformation of the cap will be resisted by the OOV. However, since the OOV is resisting bending, and therefore, resisting rotations imparted by the growth-induced torque along the intersection, we treated the OOV as an effective rotational spring [Fig. 3(a)]. Therefore, by way of a simple mechanical analogy, we model the full OC as an open spherical shallow shell, whose geometry is the same as the bilayer cap, experiencing an equivalent edge torque as shown in Fig. 3(a). The natural curvature in the cap due to differential growth, κ^{cap} , has to overcome the bending rigidity of the effective rotational spring [20], resulting in an equivalent natural curvature given by

$$\kappa^{eq} \sim \kappa^{cap} - \Gamma \frac{\Delta\theta}{\sqrt{Rh}}, \quad (2)$$

where Γ is a dimensionless ratio of bending rigidities, i.e., $\Gamma = B^{OOV}/[2B^{cap}(1+\nu)]$ ($\Gamma = 0.06$ for the OC) with bending rigidities B^{cap} and B^{OOV} of the cap and OOV, respectively, and $\Delta\theta$ is angle change along the OOV boundary layer as shown in Fig. 3(b). Here, we assumed most of the OOV deformation occurs within its boundary layer as bending [57], and the second term on the rhs of (2) describes the amount that acts to bend the OOV boundary layer.

Open spherical shallow shells undergo snapping under homogeneous positive natural curvature when the boundary tangent vector in the colatitude direction becomes approximately horizontal, which results in $\kappa^{eq}R \sim \bar{\theta}$ at the snapping [55]. Our numerical experiments here on closed spherical shells exhibit qualitatively similar behavior when the primary invagination occurs via snapping. That is, the primary invagination occurs when the colatitude-direction tangent vector at the intersection between the cap and OOV becomes approximately horizontal, which leads to $\Delta\theta \sim \alpha$ in (2) at the primary invagination. This results in a scaling law of the critical natural curvature in the cap at the primary invagination as

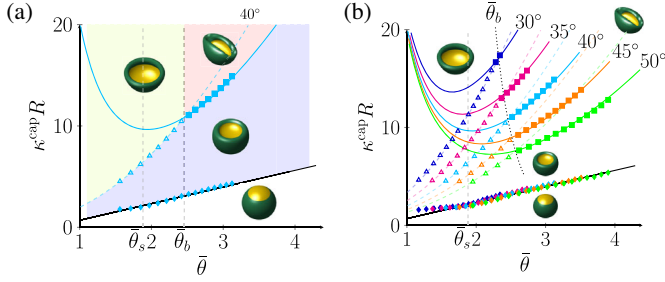


FIG. 4. (a) Phase diagram of instabilities during OC formation for varying R/h at $\alpha = 40^\circ$. The blue region denotes the invaginated cup shape, and the lime and red regions are the normal (secondary invagination) and abnormal (buckling) OC, respectively. (b) Phase diagram for varying R/h and α . For (a) and (b), the symbols refer to simulation results, with diamonds symbolizing primary invagination, triangles for secondary invagination, and squares for buckling. The lines represent the scaling law of (3), (4), and (5). The black dotted line in (b) shows the buckling transition point $\bar{\theta}_b$ of (6).

$$\kappa_1^{\text{cap}} R = a_1(1 + \Gamma)\bar{\theta} + b_1, \quad (3)$$

where a_1 and b_1 are scaling coefficients determined by our numerical simulations, which confirms the linear scaling with $\bar{\theta}$, and identifies the scaling coefficients as $a_1 = 1.55$ and $b_1 = -0.95$ [black solid line in Fig. 4(a)]. As with open shells, the primary invagination via snapping will only occur if $\bar{\theta} > \bar{\theta}_s (= [10/(1 - \nu^2)]^{1/4})$ where $\bar{\theta}_s = 1.88$ for the OC [20], in good agreement with prior work [55] as the bending-dominated boundary layer covers the entire shell for $\bar{\theta} < \bar{\theta}_s$.

Following this primary invagination, growth and development of the OC continue until a second shape-shifting event occurs, which appears to be strongly correlated to the OC geometry. Thicker shells undergo a secondary invagination, forming a deep cup that facilitates normal eye development, while slender shells lose axisymmetry, forming a shape that may hinder normal OC morphogenesis. First, we consider the onset of secondary invagination. The magnitude of the torque at the intersection between the cap and OOV continues to increase due to the continued differential growth of the ECM and IOV. The OOV is not rigid, and therefore, the torque can either bend the OOV or further bend the cap. Building on the concept of a geometric composite [58], we can consider the growing cap and OOV as separate structures and, then, determine how they will deform when combined together. The cap, when removed from the OC, would form a shallow shell that spans a characteristic distance S^{cap} [Fig. 3(c)—yellow]. The OOV, when removed from the OC, would form a deep spherical shell of radius $R' = e_{\text{OOV}}R$, which is current radius as a result of growth. From our numerical simulations, we note that the extent of the OOV boundary layer, where bending deformations are concentrated, is constant until the secondary invagination occurs. We can estimate

the characteristic span $S_{\text{bl}}^{\text{OOV}}$ of the OOV from the extent of its boundary layer [Fig. 3(c)—blue], and observe that, during secondary invagination, the OOV boundary layer increases in length and curvature. Therefore, we posit that when the span of the cap exceeds the span of the OOV boundary layer, the OC will undergo secondary invagination to account for this excess length.

The characteristic span of this OOV segment scales as $S_{\text{bl}}^{\text{OOV}} \sim R' \sin(\alpha + \theta_{\text{bl}}^{\text{OOV}})$ where $\theta_{\text{bl}}^{\text{OOV}}$ is angle subtended by the OOV boundary layer, which scales as $\theta_{\text{bl}}^{\text{OOV}} \sim \sqrt{h/R}$ for spherical shells [54]. The span of the cap scales as $S^{\text{cap}} \sim R\alpha[1 + \chi(1 + \nu)h\kappa^{\text{cap}}]$, where $\chi = [1 + m(3n - 2)]/(6mn)$ [20]. If we suppose that the critical point occurs when the spans are equivalent, i.e., $S_{\text{bl}}^{\text{OOV}} = S^{\text{cap}}$, we obtain that the critical natural curvature is proportional to the shell geometry as $\kappa^{\text{cap}} R \propto R/h$ from which the critical natural curvature in the cap at secondary invagination can be estimated as

$$\kappa_2^{\text{cap}} R \propto \frac{R}{h} = a_2 \frac{\bar{\theta}^2}{\alpha^2} + b_2, \quad (4)$$

where a_2 and b_2 are obtained from simulations to be $a_2 = 0.86$ and $b_2 = 0.22$. These parameters capture well the secondary invagination via the dashed color line in Fig. 4(a). Notably, unlike the primary invagination given by (3), the secondary invagination depends on opening angle α .

While our model predicts the morphogenetic process of OC formation via the experimentally observed [9,10] two-step (primary and secondary) invagination, it also indicates that very slender initial OC geometries will undergo an elastic instability that breaks axisymmetry, leading to abnormal OC development. This loss of the OC axisymmetry has been observed for glaucoma in newborn infants [19]. Secondary invagination occurs when the OOV boundary layer is flexible enough to bend to accommodate the excess length of the growing cap. If the OOV is too stiff, the cap must bend, instead. If we presume that the loss of axisymmetry for slender optic cups is due to a buckling instability, then the critical natural curvature can be analytically calculated via a linear stability analysis, which, for a circular plate with natural curvature κ^p and radius R^p , gives $\kappa^p h = \pm a_b (h/R^p)^2$ with $a_b = \chi(5 + 3\nu)/(1 - \nu^2)$ at the buckling instability ($a_b = 4.17$ for the OC) [20]. To connect this critical natural curvature to open spherical shallow shells, we substitute $R^p \rightarrow R\alpha$. This gives us $\kappa^{\text{eq}} R \sim a_b/\bar{\theta}^2 + 1$, which is similar to [55]. Furthermore, the spherical shell's geometry under a torque induced by natural curvature leads to $\Delta\theta \sim \sqrt{R/h}$ in (2) at the buckling instability [20]. Then, the critical natural curvature in the cap at the buckling instability is given by

$$\kappa_b^{\text{cap}} R = b_b \left(\frac{a_b}{\bar{\theta}^2} + 1 + \Gamma\alpha_2 \frac{\bar{\theta}^2}{\alpha^2} \right) + c_b, \quad (5)$$

where $\alpha_2 (= \pi - \alpha)$ is a prefactor to treat the deep OOV shell, and b_b and c_b are scaling coefficients which provide the best fit with our simulations through $b_b = 4.72$ and $c_b = -5.50$ via the solid color line in Fig. 4(a).

$$\bar{\theta}_b = \sqrt{\frac{\sqrt{4\alpha^2 b_b a_b (a_2 - \alpha_2 b_b \Gamma)} + \alpha^4 (c_b - b_2 + b_b)^2 + \alpha^2 (c_b - b_2 + b_b)}{2(a_2 - \alpha_2 b_b \Gamma)}}, \quad (6)$$

where $\bar{\theta}_b = 2.46$ is calculated at $\alpha = 40^\circ$, in agreement with the numerical results ($\bar{\theta}_b = 2.51$).

Similar to the various R/h in biological situations, it is natural to think that the opening angle will also vary with diverse biological cues. The simulation results with various opening angles for a wide range from 30° to 50° are plotted on a phase diagram in Fig. 4(b) which fully characterizes the instability-induced shape morphing of the OC during its morphogenesis for a variety of initial geometries, showing that the proposed scaling laws work well for all α . Above the value of $\bar{\theta}_b$, denoted as the dashed black line via (6), the final OC shape is abnormal for each α .

In summary, we revealed the significant role that elastic instabilities play during OC morphogenesis. Because our model is predictive based on the initial geometry, we hope that our study will motivate experimental efforts to measure radius R , thickness h , and opening angle α of the initial OV to investigate their effects on OC morphogenesis and to verify the accuracy of our model predictions.

J.-H. L., H. S. P., and D. P. H. gratefully acknowledge financial support from the National Science Foundation through Grant No. CMMI-1824882.

* parkhs@bu.edu

† dpholmes@bu.edu

- [1] E. J. Pearl, J. Li, and J. B. Green, Cellular systems for epithelial invagination, *Phil. Trans. R. Soc. B* **372**, 20150526 (2017).
- [2] S. E. Skalicky, A. J. White, J. R. Grigg, F. Martin, J. Smith, M. Jones, C. Donaldson, J. E. Smith, M. Flaherty, and R. V. Jamieson, Microphthalmia, anophthalmia, and coloboma and associated ocular and systemic features: Understanding the spectrum, *JAMA Ophthalmol.* **131**, 1517 (2013).
- [3] H. Lee, R. Khan, and M. O'Keefe, Aniridia: Current pathology and management, *Acta Ophthalmol.* **86**, 708 (2008).
- [4] C.-J. Zhou, A. Molotkov, L. Song, Y. Li, D. E. Pleasure, S. J. Pleasure, and Y.-Z. Wang, Ocular coloboma and dorsoventral neuroretinal patterning defects in Lrp6 mutant eyes, *Dev. Dyn.* **237**, 3681 (2008).

As our numerical experiments indicate that both secondary invagination and symmetry-breaking buckling cannot occur for the same initial geometry, the intersection between (4) and (5) gives us the transition point from secondary invagination to buckling as

- [5] S. Fuhrmann, Eye morphogenesis and patterning of the optic vesicle, in *Current Topics in Developmental Biology* (Elsevier, New York, 2010), Vol. 93, pp. 61–84.
- [6] D. Rosen and N. Mahabadi, Embryology, optic cup, in *StatPearls [Internet]* (StatPearls Publishing, Florida, 2019).
- [7] R. Hendrix and J. Zwaan, Changes in the glycoprotein concentration of the extracellular matrix between lens and optic vesicle associated with early lens differentiation, *Differentiation (Berlin)* **2**, 357 (1974).
- [8] C. D. Bryan, M. A. Casey, R. L. Pfeiffer, B. W. Jones, and K. M. Kwan, Optic cup morphogenesis requires neural crest-mediated basement membrane assembly, *Development* **147**, dev181420 (2020).
- [9] A. Oltean, J. Huang, D. C. Beebe, and L. A. Taber, Tissue growth constrained by extracellular matrix drives invagination during optic cup morphogenesis, *Biomech. Model. Mechanobiol.* **15**, 1405 (2016).
- [10] H. S. Hosseini and L. A. Taber, How mechanical forces shape the developing eye, *Prog. Biophys. Molec. Biol.* **137**, 25 (2018).
- [11] R. Adler and M. V. Canto-Soler, Molecular mechanisms of optic vesicle development: Complexities, ambiguities and controversies, *Dev. Biol.* **305**, 1 (2007).
- [12] J. Hyer, J. Kuhlman, E. Afif, and T. Mikawa, Optic cup morphogenesis requires pre-lens ectoderm but not lens differentiation, *Dev. Biol.* **259**, 351 (2003).
- [13] M. Eiraku, N. Takata, H. Ishibashi, M. Kawada, E. Sakakura, S. Okuda, K. Sekiguchi, T. Adachi, and Y. Sasai, Self-organizing optic-cup morphogenesis in three-dimensional culture, *Nature (London)* **472**, 51 (2011).
- [14] T. Nakano, S. Ando, N. Takata, M. Kawada, K. Muguruma, K. Sekiguchi, K. Saito, S. Yonemura, M. Eiraku, and Y. Sasai, Self-formation of optic cups and storable stratified neural retina from human ESCs, *Cell Stem Cell* **10**, 771 (2012).
- [15] K. M. Kwan, H. Otsuna, H. Kidokoro, K. R. Carney, Y. Saijoh, and C.-B. Chien, A complex choreography of cell movements shapes the vertebrate eye, *Development* **139**, 359 (2012).
- [16] W. A. Harris and V. Hartenstein, Neuronal determination without cell division in *Xenopus* embryos, *Neuron* **6**, 499 (1991).
- [17] J. R. Martinez-Morales and J. Wittbrodt, Shaping the vertebrate eye, *Curr. Opin. Genet. Dev.* **19**, 511 (2009).
- [18] S. Okuda, N. Takata, Y. Hasegawa, M. Kawada, Y. Inoue, T. Adachi, Y. Sasai, and M. Eiraku, Strain-triggered

- mechanical feedback in self-organizing optic-cup morphogenesis, *Sci. Adv.* **4**, eaau1354 (2018).
- [19] K. T. Richardson, Optic cup symmetry in normal newborn infants, *Invest. Ophthalmol. Visual Sci.* **7**, 137 (1968), <https://iovs.arvojournals.org/article.aspx?articleid=2128431>.
- [20] See Supplemental Material at <http://link.aps.org/supplemental/10.1103/PhysRevLett.127.138102> for a detailed derivation, which includes Refs. [21–28].
- [21] R. A. Sauer and T. X. Duong, On the theoretical foundations of thin solid and liquid shells, *Math. Mech. Solids* **22**, 343 (2017).
- [22] F. Roohbakhshan and R. A. Sauer, Efficient isogeometric thin shell formulations for soft biological materials, *Bio-mech. Model. Mechanobiol.* **16**, 1569 (2017).
- [23] E. Efrati, E. Sharon, and R. Kupferman, Elastic theory of unconstrained non-Euclidean plates, *J. Mech. Phys. Solids* **57**, 762 (2009).
- [24] W. T. Koiter and J. G. Simmonds, Foundations of shell theory, in *Theoretical and Applied Mechanics* (Springer, New York, 1973), pp. 150–176.
- [25] M. Pezulla, N. Stoop, X. Jiang, and D. P. Holmes, Curvature-driven morphing of non-Euclidean shells, *Proc. R. Soc. A* **473**, 20170087 (2017).
- [26] A. Lucantonio, P. Nardinocchi, and M. Pezulla, Swelling-induced and controlled curving in layered gel beams, *Proc. R. Soc. A* **470**, 20140467 (2014).
- [27] M. Pezulla, G. P. Smith, P. Nardinocchi, and D. P. Holmes, Geometry and mechanics of thin growing bilayers, *Soft Matter* **12**, 4435 (2016).
- [28] W. T. Koiter and A. Van Der Heijden, *WT Koiter's Elastic Stability of Solids and Structures* (Cambridge University Press, Cambridge; New York, NY, USA 2009).
- [29] S. Höhn, A. R. Honerkamp-Smith, P. A. Haas, P. K. Trong, and R. E. Goldstein, Dynamics of a *Volvox* Embryo Turning Itself Inside Out, *Phys. Rev. Lett.* **114**, 178101 (2015).
- [30] P. A. Haas, S. M. H. Hohn, A. R. Honerkamp-Smith, J. B. Kirkegaard, and R. E. Goldstein, The noisy basis of morphogenesis: Mechanisms and mechanics of cell sheet folding inferred from development variability, *PLOS Biol.* **16**, e2005536 (2018).
- [31] P. A. Haas and R. E. Goldstein, Morphoelasticity of large bending deformations of cell sheets during development, *Phys. Rev. E* **103**, 022411 (2021).
- [32] G. Chagnon, M. Rebouah, and D. Favier, Hyperelastic energy densities for soft biological tissues: A review, *J. Elast.* **120**, 129 (2015).
- [33] S. Budday, G. Sommer, C. Birkl, C. Langkammer, J. Haybaeck, J. Kohnert, M. Bauer, F. Paulsen, P. Steinmann, E. Kuhl *et al.*, Mechanical characterization of human brain tissue, *Acta Biomater.* **48**, 319 (2017).
- [34] E. K. Rodriguez, A. Hoger, and A. D. McCulloch, Stress-dependent finite growth in soft elastic tissues, *J. Biomech.* **27**, 455 (1994).
- [35] A. Goriely, *The Mathematics and Mechanics of Biological Growth* (Springer, New York, 2017), Vol. 45.
- [36] E. Kuhl, Growing matter: A review of growth in living systems, *J. Mech. Behav. Biomed. Mater.* **29**, 529 (2014).
- [37] V. A. Lubarda and A. Hoger, On the mechanics of solids with a growing mass, *Int. J. Solid Struct.* **39**, 4627 (2002).
- [38] T. X. Duong, F. Roohbakhshan, and R. A. Sauer, A new rotation-free isogeometric thin shell formulation and a corresponding continuity constraint for patch boundaries, *Comput. Methods Appl. Mech. Eng.* **316**, 43 (2017).
- [39] A. V. De Reuck and J. Knight, *Colour Vision: Physiology and Experimental Psychology* (John Wiley & Sons, New York, 2009), Vol. 965.
- [40] S. R. Hilfer, R. C. Brady, and J.-J. W. Yang, Intracellular and extracellular changes during early ocular development in the chick embryo, in *Ocular Size and Shape Regulation During Development* (Springer, New York, 1981), pp. 47–78.
- [41] H. S. Hosseini, D. C. Beebe, and L. A. Taber, Mechanical effects of the surface ectoderm on optic vesicle morphogenesis in the chick embryo, *J. Biomech.* **47**, 3837 (2014).
- [42] A. Djellouli, P. Marmottant, H. Djeridi, C. Quilliet, and G. Couplier, Buckling Instability Causes Inertial Thrust for Spherical Swimmers at All Scales, *Phys. Rev. Lett.* **119**, 224501 (2017).
- [43] A. G. Holzapfel, *Nonlinear Solid Mechanics II* (John Wiley & Sons, New York, 2000).
- [44] M. Ben Amar and A. Goriely, Growth and instability in elastic tissues, *J. Mech. Phys. Solids* **53**, 2284 (2005).
- [45] G. Xu, P. S. Kemp, J. A. Hwu, A. M. Beagley, P. V. Bayly, and L. A. Taber, Opening angles and material properties of the early embryonic chick brain, *J. Biomech. Eng.* **132**, 011005 (2010).
- [46] E. Uchio, S. Ohno, J. Kudoh, K. Aoki, and L. T. Kisielewicz, Simulation model of an eyeball based on finite element analysis on a supercomputer, *British Journal of Ophthalmology* **83**, 1106 (1999).
- [47] I. A. Sigal, J. G. Flanagan, and C. R. Ethier, Factors influencing optic nerve head biomechanics, *Invest. Ophthalmol. Visual Sci.* **46**, 4189 (2005).
- [48] E. A. Bassett, T. Williams, A. L. Zacharias, P. J. Gage, S. Fuhrmann, and J. A. West-Mays, *Ap-2 α* knockout mice exhibit optic cup patterning defects and failure of optic stalk morphogenesis, *Human Molecular Genetics* **19**, 1791 (2010).
- [49] L.-Y. Wu, M. Li, D. R. Hinton, L. Guo, S. Jiang, J. T. Wang, A. Zeng, J. B. Xie, M. Snead, C. Shuler *et al.*, Microphthalmia resulting from *Msx2*-induced apoptosis in the optic vesicle, *Invest. Ophthalmol. Visual Sci.* **44**, 2404 (2003).
- [50] Y. Ishii, K. Weinberg, I. Oda-Ishii, L. Coughlin, and T. Mikawa, Morphogenesis and cytodifferentiation of the avian retinal pigmented epithelium require down-regulation of Group B1 Sox genes, *Development* **136**, 2579 (2009).
- [51] F. Müller, H. Rohrer, and A. Vogel-Höpker, Bone morphogenetic proteins specify the retinal pigment epithelium in the chick embryo, *Development* **134**, 3483 (2007).
- [52] T. Pandit, V. K. Jidigam, C. Patthey, and L. Gunhaga, Neural retina identity is specified by lens-derived BMP signals, *Development* **142**, 1850 (2015).

- [53] Y. Hasegawa, N. Takata, S. Okuda, M. Kawada, M. Eiraku, and Y. Sasai, Emergence of dorsal-ventral polarity in esc-derived retinal tissue, *Development* **143**, 3895 (2016).
- [54] F. I. Niordson, *Shell Theory* (Elsevier, New York, 2012).
- [55] M. Pezzulla, N. Stoop, M. P. Steranka, A. J. Bade, and D. P. Holmes, Curvature-Induced Instabilities of Shells, *Phys. Rev. Lett.* **120**, 048002 (2018).
- [56] D. P. Holmes, J.-H. Lee, H. S. Park, and M. Pezzulla, Nonlinear buckling behavior of a complete spherical shell under uniform external pressure and homogenous natural curvature, *Phys. Rev. E* **102**, 023003 (2020).
- [57] E. Efrati, E. Sharon, and R. Kupferman, Buckling transition and boundary layer in non-Euclidean plates, *Phys. Rev. E* **80**, 016602 (2009).
- [58] M. Pezzulla, S. A. Shillig, P. Nardinocchi, and D. P. Holmes, Morphing of geometric composites via residual swelling, *Soft Matter* **11**, 5812 (2015).